BINARY COLLISIONS AND COALESCENCE OF DROPLETS IN LOW-PRESSURE FUEL INJECTOR

by

Fatma B. M. AHMED[a*], ***Nobuyuki KAWAHARA***[b], ***and Eiji TOMITA***[b]

[a]Department of Physics, Faculty of Science, Aswan University, Aswan, Egypt
[b]Department of Mechanical Engineering, Okayama University, Kita, Okayama, Japan

Original scientific paper
https://doi.org/10.2298/TSCI191120185A

The phenomena of binary collisions and coalescence of droplets was investigated from experimental studies but still are missing from real applications such as from fuel injector. The main purpose of the current study is to investigate the phenomena of binary collisions and coalescence of droplets from a practical port fuel injector. To accomplish this, direct microscopic images are taken from high speed video camera coupled with a long-distance microscope and Barlow lens using the backlighting method. Experimental optimization of the spatial resolution and the depth -of -field of the long-distance microscope and Barlow lens are achieved. Experimental results from the direct microscopic images are compared with predictions from empirical equations for different collision regimes. Droplet sizes and velocities of experimental coalescence droplets from collisions are compared with the values predicted by the equations. The main results of this study are: The probability of collision and coalescence is very low in a port fuel injector. The tangential velocity components of small droplets play an essential role in shape deformation during collisions and coalescence of the droplets. The previous published empirical equations to calculate dimensionless parameters, the Weber number, the droplet diameter ratio, and impact parameter are applicable to the coalescence of droplets in a port fuel injector.

Key words*: direct microscopic image, collision, coalescence, port fuel injector, droplet collision regimes, high speed video camera*

Introduction

Fluid droplets dynamics are very important in many natural processes and engineering applications. Rain, various coating processes, spray painting, and the fuel sprays combustion are only some examples. Although the dynamics of a single droplet and its interactions with the surrounding flow is often taken the attention, in an actual spray many droplets are present. Sometimes the average distance between droplets is a little lower than droplet diameters, as a result a typical droplet will not behave as a single droplet, and it will be strongly affected by the neighbouring droplets and to some extent by all droplets in the spray. For a

[*] Corresponding author, e-mail: Fatmaowny@yahoo.com

large number of droplets per unit volume it is vital to account for the droplets and their collective effect on the flow [1]. The binary droplet collisions phenomena become more complicated in real applications, especially those occurring in internal combustion engines of limited volume. Coalescence, the phenomenon in which two liquid droplets combine into a single droplet through a collision, is a fundamental feature of many natural processes and is attracting increased attention. Coalescence occurs at low Weber number conditions.

At the port fuel injector (PFI) exit, (where there is large number of droplets per unit volume and as a sequences high collisions probability), droplet coalescence affects the sizes and spatial distribution of droplets and can, therefore, affect evaporation, combustion, and pollutant formation. Therefore, quantitative and qualitative understanding of droplet interactions, including binary droplet collisions, is very important. The researchers of spray combustion have paid great attention to the outcome of binary liquid droplets collisions, *e.g.*, water, hydrocarbons, *etc.*, to understand collision physics [2-11] or utilize the measured data in the numerical modelling of fuel sprays [12-15]. Most of the previous experiments on droplet collision have been conducted with fundamental experimental studies of two droplets in collision configuration, *i.e.*, generated droplets to collision each other and the collision results expected to be valid for liquid droplets with the same dimensionless parameters [2, 4, 16, 17]. The collision outcome is divided into five main regimes [3, 4]: I – coalescence that come after a little deformation, II – bouncing, III – coalescence come after a substantial deformation, IV – separation that followed temporary coalescence for head-on collisions, and V – separation that followed coalescence for off-centre collisions

The aforementioned transitions are classified according to collision Weber number, the ratio of droplet size, and an impact parameter, which are the key parameters for determining the behaviour in a collision between two liquid droplets [2-4]. A wide variety of scenarios have been proposed [2, 4, 17, 18], to show the characteristic transitions between these different regimes.

Ashgriz and Poo [2] proposed a theoretical model to predict reflexive and stretching separation. The studies have been extended to hydrocarbon droplets for the spray combustion application [3]. Jiang *et al*. [17] performed a systematic and extensive investigation on the hydrocarbon droplets collision and compared the results with that of the water droplets collision. They found that hydrocarbon droplets behaviour is extremely different and more complicated than that of water droplets. There were two more outcome regimes (I and II) for hydrocarbon droplets in addition to the three outcome regimes (III-V) for water droplets. They then introduced a theoretical model to include the effect of viscosity and energy dissipation. Qian and Law [4] showed that for different liquids, these five regimes could be unified through varying the liquid properties and the gas between the droplets. Also, their results showed that the collision outcome was shifted as a result of the presence of the gaseous hydrocarbons. There are numerous numerical and experimental studies concerning the collision of various hydrocarbons, such as two droplets of propanol [5], two droplets of ethanol [19], two droplets of diesel [12], a droplet of methanol and droplet of water [20], droplet of diesel and droplet of water [21], and two droplets of tetradecane [18]. However, the most studies focus mainly on the collision regimes, the dynamics, and the formation of satellite droplet, without involving combustion. Recently, more theoretical and modelling studies of collision dynamics and mixing have been performed [22-29], also on the effect of viscosity on droplets interaction [13, 15, 30, 31].

Survey in previous research revealed that direct experiments on droplet collisions in the region near the nozzle exit of practical PFI (*i.e.*, detecting collisions from the breakup of a liquid fuel column) have never been attempted due to the very small region in which the phenomena occur. The probability that two droplets will collide depends on their velocities and directions of motion, as well as on the local void fraction within the spray. Thus, the frequency of droplet collisions is greatest in the dense spray regions close to the nozzle.

The purpose of the present experimental study is to utilize the high spatial and temporal resolution of an ultra-high-speed video camera coupled with a long-distance microscope and Barlow lens to elucidate the binary collision and coalescence mechanisms of droplets during the breakup of a liquid column in a PFI. To accomplish this, two main problems must be solved. The first is to determine the resolution and depth of the field of the optical system. The second is to validate the experimental droplet coalescence results with theoretical transition curves based on experimentally determined relative velocities and droplet sizes.

Materials and methods

Port fuel injector

The PFI used in this study was a prototype that was fabricated specifically for research use and not for commercial use. This injector made by Mitsubishi Electric Corporation as well as the multi-hole injector. The PFI schematic diagram used in this study is shown in fig. 1. The injector cavity type is tapered with a nozzle angle of 21°. The injector nozzle hole diameter, d, is 0.2 mm, the nozzle pitch diameter, D, is 2.13 mm, and the nozzle plate thickness is 0.12 mm. This injector has 10 nozzles, so that the spray is very dense just under the nozzle. It is very difficult to analyse the spray from just one nozzle because the shadows of the 10 nozzle sprays overlap with each other. Therefore, an attaching separation plate was used to isolate the spray from one nozzle (as shown in fig. 1) so that a spray of the single nozzle can come over the field of view, and the others run out of the visible field. The separation plate is very thin to observe the nozzle just from 0.5 mm below.

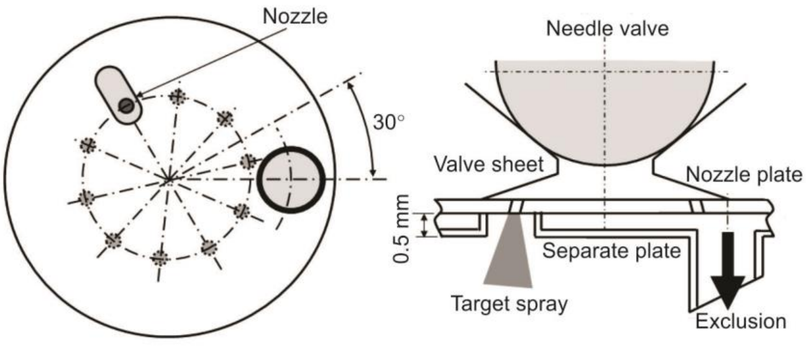

Figure 1. Schematic diagram of PFI

Experimental set-up

A schematic for the experimental set-up of the direct microscopic image is shown in fig. 2. The system includes a PFI, a constant-volume chamber, an electronic control circuit, a fuel supply system, and a high speed video camera system. The constant-volume chamber interior diameter is 180 mm and the height is 350 mm. The chamber has a transparent window at each side for optical observation. The PFI was mounted at the constant-volume chamber upper plate. A system of fuel supply with a pressure controller was used, in which a fuel was

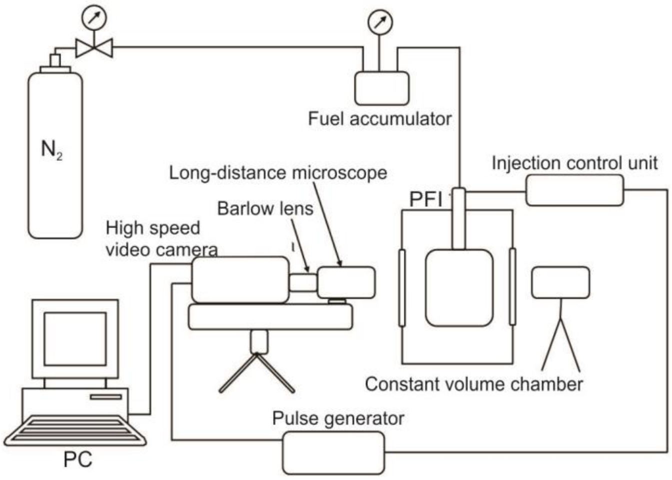

Figure 2. Schematic diagram of the experimental set-up

contained in an accumulator pressurized by nitrogen. A pulse generator was used to control the injection signal and the signal was transmitted simultaneously to the injector and high speed video camera. The dry solvent was used as a fuel in this study. The physical properties of dry solvent are similar to those of gasoline: surface tension, $\sigma = 25$ mN/m, density, ρ = 765 kg/m^3, and kinematic viscosity, ν = 1.032 mm^2/s. However, the dry solvent volatility is lower than that of gasoline, the dry solvent was often used in experimental investigations in which evaporation must be limited. The injection duration was fixed at 3.5 ms. The injection pressure was 0.3 MPa, with stagnant conditions of the surroundings and ambient atmospheric pressure.

The direct microscopic imaging system

The imaging apparatus is illustrated in fig. 2. This system is consisted of a high speed video camera (Shimadzu Hyper Vision HPV-1), a Barlow lens, and a long-distance microscope, with continuous light provided by a strong metal halide lamp. The high speed video camera is the most effective device to visualize and record high speed phenomena. The high speed video camera enables high resolution (312 × 260) and high speed imaging (maximum recording rate of 1 Mfps). The camera has a minimum exposure time of 0.125 μs and a gain factor between 1 and 50. The maximum number of frames that can be captured is 102. The long-distance microscope is a Maksutov-Cassegrain catadioptric microscope utilizable at working distances ranging from 196 to 306 mm. The main components of this microscope are convex front lens, rear concave mirror, and another mirror. The microscope was specially designed and manufactured for high speed microscopic visualization of atomization processes. A Barlow lens adjusts the effective focal ratio for the optical systems, and hence magnifying images. A strong metal halide lamp is used as a uniform backlight source. The photographic images are 10 bit black and white images. To obtain an accurate quantification detailed of the spray characteristics from the images, it is very important to distinguish the spray image from the background and define the boundary of spray. A threshold is used to identify the atomization process outline in the images. Figure 3 shows a typical unprocessed example of a macro-

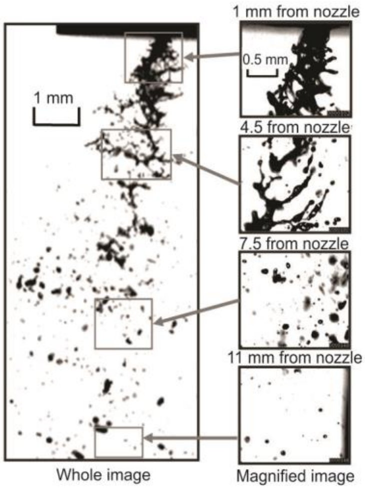

Figure 3. Whole and magnified image

scopic whole image of spray and a magnified image using the Barlow lens. Some qualitative observations can be made from this image.

Spatial resolution and depth of field

To optimize the spatial resolution and depth of field, a test target with equally spaced (1 mm) dark vertical and horizontal lines is used. The depth of field is defined as the range of motion of an object or specimen along the optical axis (focal plane) without impacting the clarity of viewing. In other words, the depth of field specifies how much an object or specimen can move and remain clear. The depth of field is quantified by imaging the test target at different distances from the focal plane of a long-distance microscope. The focal plane of the test target is adjusted, and images are recorded at different positions from the focal plane. At each position, the densities (pixel numbers) of dark lines are evaluated by image processing. Figure 4 shows the depth of field at a focal plane 225 mm from the long-distance microscope, and this point is considered to be the zero point. As the figure indicates, images at positions varying from –200 μm to +100 μm (negative values denoting the direction toward the microscope and positive values denoting the direction away from the microscope) retain an acceptable focus and the same density. Hence, at that position (225 mm), the depth of the field is close to 300 μm. The spatial resolution of the imaging is determined from an image positioned in the focal plane (~depth of field) in which the number of pixels between the centre lines of any two parallel dark lines is equivalent to one millimetre. The corresponding resolution is calculated from this, and the image resolution at that position (225 mm) is found to be 6.8 μm.

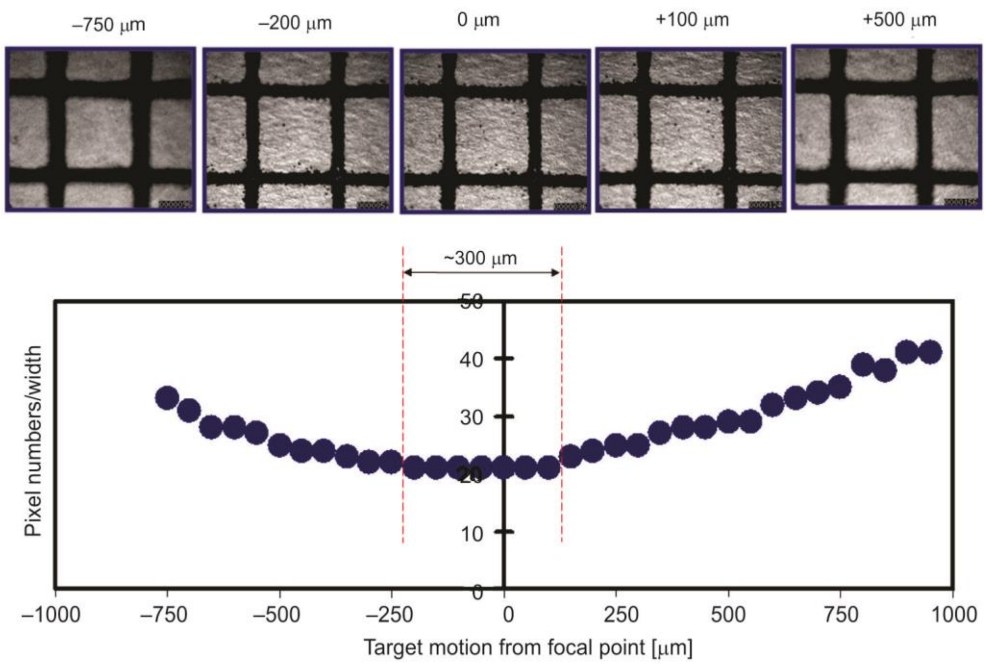

Figure 4. Determination depth of field, 225 mm from long-distance microscope, high speed video camera recording rate and the exposure time were 250 kfps and 2 , respectively

Droplet collision theories and theoretical transition curves

Important parameters determination

The collision phenomena is characterized by three important dimensionless parameters, the Weber number, the droplet diameter ratio, Δ, and impact parameter, B, which are defined by [2]:

$$\mathrm{We} = \frac{\rho_\mathrm{f} d_2 u_{12}^2}{\sigma_\mathrm{f}}, \quad \Delta = \frac{r_2}{r_1}, \quad B = \frac{X}{r_1 + r_2} \tag{1}$$

where the subscripts 1 and 2 indicate the larger and smaller droplets, respectively, ρ_f – the liquid droplet density, σ_f – the surface tension, and d and u are the droplet diameter and velocity, respectively. The impact parameter X is defined as the distance between the droplet centres in the normal direction to the relative velocity u_{12}, as shown in fig. 5. The quantity B is the dimensional impact parameter, which varies from 1 to 0.

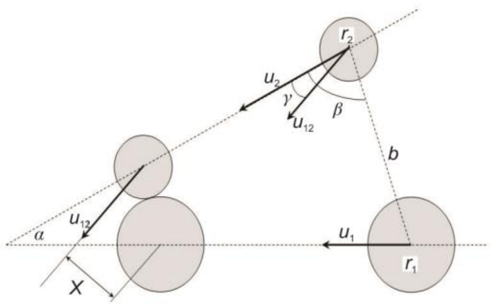

Figure 5. Geometric parameters of droplets collision

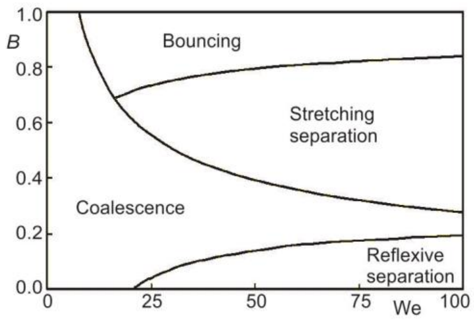

Figure 6. Schematic of droplet collision regimes [4]

Theoretical transition curves

A schematic diagram of the droplet collision regimes as a function of the collision Weber number and impact parameters is shown in fig. 6.

The following empirical equation is used to calculate the critical impact parameter [32], which divides coalescence from stretching separation:

$$B = \left(\frac{24}{5\mathrm{We}}\right)^{1/2} \frac{\left(1+\Delta^3\right)^{11/6}}{\left(1+\Delta\right)\Delta^{5/2}} \left[1 + \Delta^2 - \left(1+\Delta^3\right)^{2/3}\right]^{1/2} \tag{2}$$

Another empirical equation is used to calculate the critical Weber number impact plot that defines the region between coalescence and reflexive separation [2]:

$$\mathrm{We} > \frac{3\left[7\left(1+\Delta^3\right)^{2/3} - 4\left(1+\Delta^2\right)\right]\Delta\left(1+\Delta^3\right)^2}{\left(\Delta^6\eta_1 + \eta_2\right)} \tag{3}$$

where $\eta_1 = 2(1 - \xi^2)(1 - \xi^2)^{1/2} - 1$, $\eta_2 = 2(\Delta - \xi)^2(\Delta^2 - \eta^2)^{1/2} - \Delta^3$, and $\xi = B(1 + \Delta)$.

To determine the boundary for bouncing, an empirical equation is used to predict the occurrence of coalescence [19]:

$$\mathrm{We} \geq \frac{\Delta\left(1+\Delta^2\right)\left(4\phi' - 12\right)}{X_1\left\{\cos\left[\sin^{-1}\left(B\right)\right]\right\}^2} \tag{4}$$

where ϕ' is a shape factor with a value 3.351, and X_1 is defined by:

$$X_1 = \begin{cases} 1 - 0.25(2-\tau)^2(1+\tau) \text{.....for } \omega > r_1 \\ 0.25\tau^2(3-\tau) \text{..................for } \omega \leq r_1 \end{cases} \tag{5}$$

with $\tau = (1 - B)(1 + \Delta)$ and $\omega = (r_1 + r_2)(1 - B)$

In the statistical approach to predicting a coalescence collision event, if two droplets permanently coalescence [33], the velocity and diameter of the combined droplet are calculated from:

$$\vec{U}_{\text{new}} = \frac{m_1\vec{u_1} + m_2\vec{u_2}}{m_1 + m_2}, \quad D_{\text{new}} = \left(D_1^3 + D_2^3\right)^{1/3} \tag{6}$$

Results and discussion

Experiments were performed at different positions close to the nozzle exit to study the dynamics of collisions and coalescence of droplets from the atomization process of the PFI. The probability of capturing an image containing a collision phenomenon from the set of images taken during the experiment is low at each position from the nozzle exit due to the low exit flow velocity of this type of injector. The probabilities are roughly 0.06, 0.06, 0.15, 0.03, 0.02, and 0.02% at the respective distances of 3.5, 4.5, 5, 6, 8, and 10 mm from the nozzle exit. The droplet diameter, the droplet velocity, and impact parameter are required to calculate the Weber number and the droplet diameter ratio for collision or coalescence. To obtain these values, it is crucial to visualize the droplets clearly at an appropriate magnification. The exposure time and frame rate were adjusted to get the best results. The exposure time was held constant at 200 μs during this experiment. The frame rate should be adjusted to enable us to track particular droplets in successive images. When the frame rate is slow compared to the droplet velocity, the droplet may be lost in the next image and the velocity cannot be calculated. In this experiments the frame rate was 250 kfps. Figure 7 presents examples of the time evolution mechanism of the coalescence process from the collision of the droplets, including images with different diameter ratios (a) $\Delta = 0.875$, (b) $\Delta = 0.500$, (c) $\Delta = 0.556$, and (d) $\Delta = 0.583$, and at different positions from the nozzle exit, 3.5 mm in figs. 7(a) and 7(b), and 4.5 mm in figs. 7(c) and 7(d). As can be seen, different collision responses were observed in our experiments. Droplets approaching each other collided, start deforming, and coalesced to form a single larger droplet, which oscillated, figs. 7(b) and 7(d), or rotated (figs. 7(a) and 7(c), to dissipate the collision induced energy via viscous damping and restoring surface tension forces which cause a pressure difference between its inner and outer regions. The experiments showed that coalescence is often highly unstable during the early stages. After a characteristic time interval, the amplitude of these oscillations and rotations decay, and the droplet displays a steady-state shape.

When Weber number is of small value, after two droplets contact, the merged droplet deforms slightly and finally returns to an ellipsoidal shape, as is shown in figs. 7(b) and 7(d). If the time after collision is long enough, the ellipsoidal shape would finally oscillate into a spherical shape. Surface tension is dominated to prevent the collision complex from breaking up, and the kinetic energy of two droplets is too small to split them apart, this type of collision is called *coalescence collision*. As shown in fig. 7 the increased impact parameter induces the rotation of collision complex, but the surface tension effects prevents it from breaking up after oscillating. The free-flight distance of the droplets before the collision is sufficiently short so that the droplet velocity and trajectory and do not show significant change. The trajectory angle variation alters the collision energy through the change of relative velocity between the droplets, and this affects the shape of the coalescence deformation, which may be either an oscillation or a rotation. For non-rotational shapes, it was found that the smaller droplets have a larger tangential velocity than do the larger droplets. It can thus be concluded that the tangential velocity components of smaller droplets play a vital role in collisions and coalescence.

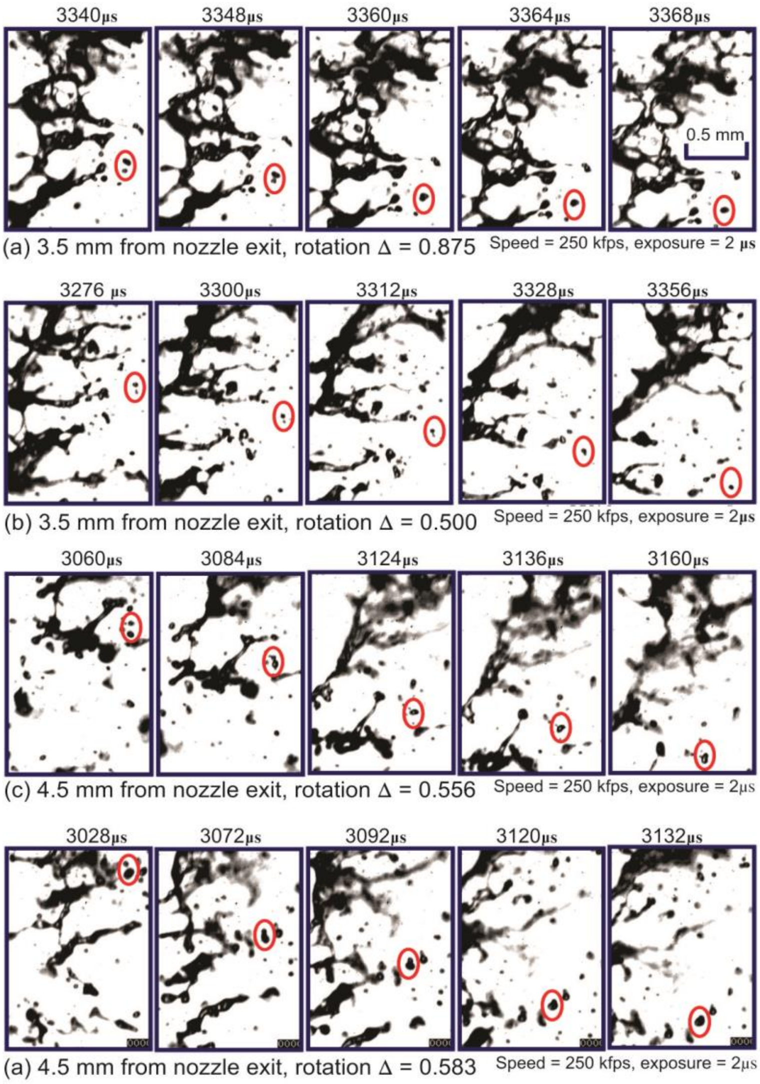

Figure 7. Visualization of collision and coalescence droplet at different position from nozzle exit and varies droplets diameter ratio

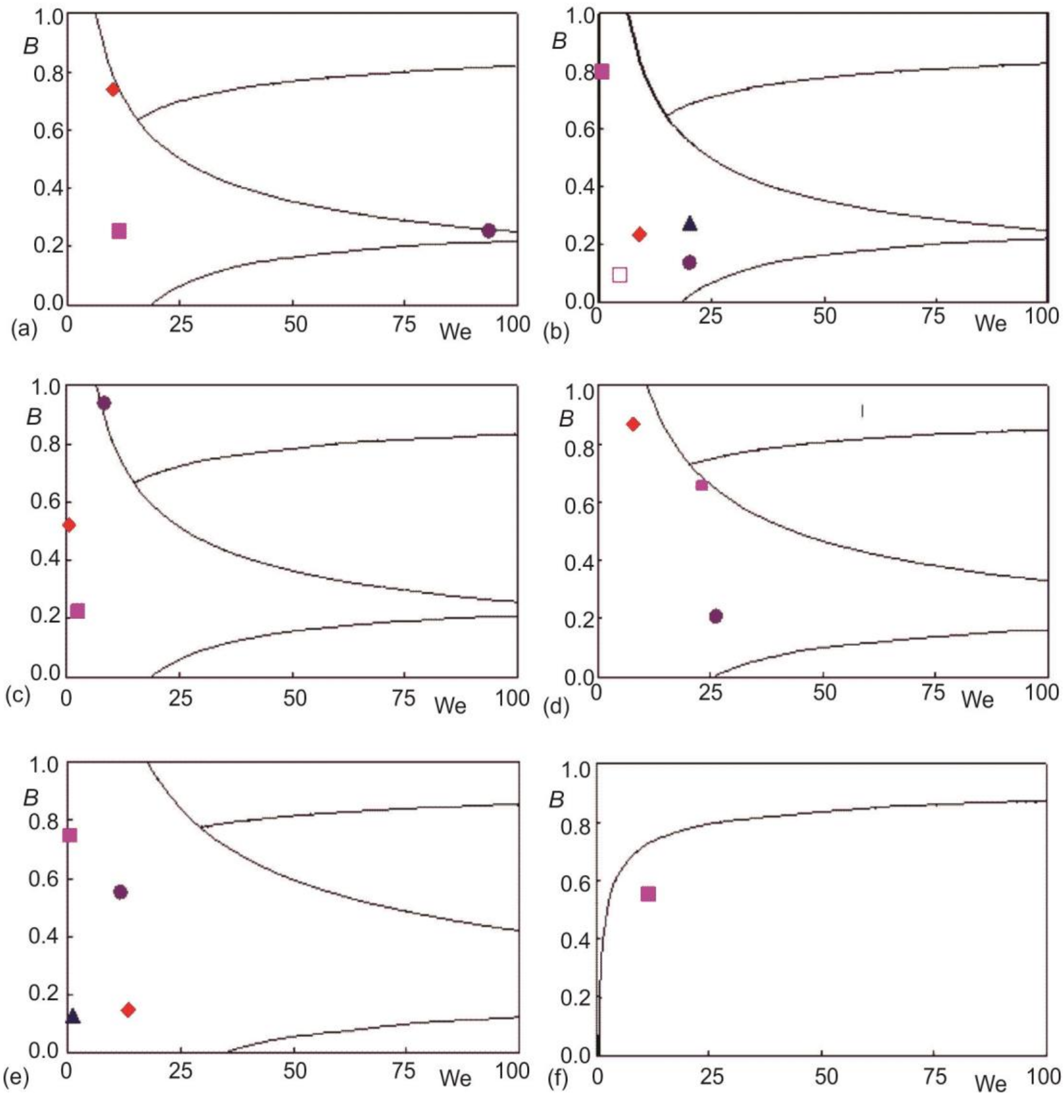

Figure 8. Droplet collision and coalescence outcome for the various droplet and position from nozzle exit: (a) Δ = 0.9 ~ 1, ■ rotation at 8 mm, ● at 5 mm, ♦ rotation at 4.5 mm, (b) Δ = 0.8~0.9, ■ at 3.5 mm, ♦ rotation at 3.5 mm, ● rotation at 5 mm, ▲ at 5 mm, ■ at 3.5 mm, (c) Δ = 0.7~0.8, ■ at 6 mm, ● rotation at 5 mm, ♦ at 3.5 mm, (d) Δ = 0.5~0.6, ■ rotation at 5 mm, ● at 4.5 mm, ♦ rotation at 4.5 mm, (e) Δ = 0.4~0.5, ■ at 3.5 mm, ♦ at 5 mm, ● rotation at 10 mm, ▲ rotation at 4.5 mm, and (f) Δ = 0.2~0.3, ■ at 4.5mm

Figure 8 compares the qualitative experimental regime results map with predictions obtained from the equations as a function of Weber number and impact parameters for different diameter ratios and positions and various coalescence deformation shapes. Figure 8 shows the regions of different collision regimes in terms of the impact parameter X and Weber number for the range of $0 \leq B \leq 1$ and $0 \leq \mathrm{We} \leq 100$. Generally speaking, there is good agreement between the experimental results and the predictions from the equations over the range of positions, diameter ratios, and coalescence deformation shapes considered here. It is therefore concluded that these equations will apply to a PFI under the present circumstances.

Table 1 lists the diameters and velocities of coalescence droplets obtained from the experimental observations and the equations. It can be seen that there is good agreement between the experimental and predicted results for droplet diameter and velocity in different positions.

Table 1. Comparison between resulting size and velocity of coalescence droplets from experimental and predicated equations

Δ	We	*B*	*d* [μm]		*V* [ms^{-1}]	
			Experimental	Predicated	Experimental	Predicated
1.000	11.6	0.253	86	84	13.02	13.36
0.875	8.9	0.236	69	65	13.05	12.87
0.833	0.6	0.798	48	48	12.74	11.91
0.778	2.6	0.222	82	84	12.68	13.72
0.714	8.4	0.940	65	63	11.46	11.60
0.600	23.3	0.656	41	44	10.87	11.96
0.583	26.4	0.209	103	101	14.09	13.24
0.556	8	0.869	79	75	12.19	13.35
0.500	0.6	0.747	41	43	10.72	10.61
0.429	1.1	0.125	55	57	13.31	13.29
0.273	4.5	0.537	87	87	11.06	11.08

Conclusions

An ultra-high-speed video camera coupled with a long-distance microscope and a Barlow lens was used to obtain direct microscopic images to investigate collisions and coalescence during the atomization process close to the nozzle of practical PFI injector. Experimental optimization of the spatial resolution and depth of field of the long-distance microscope and Barlow lens was carried out. Experimental results from the direct microscopic images were compared with predictions obtained from the empirical equations for different collision regimes. The sizes and velocities of experimental coalescence droplets from collisions were compared with those predicted by the equations. The following conclusions were obtained:

- The spatial resolution of the imaging can be determined and optimized from an image positioned in the focal plane. The probability of collision and coalescence during the atomization process of a PFI is low.
- The experimental results indicated that the tangential velocity components of the smaller droplets play a vital role in the shape deformation of the collision and the coalescence of the droplets.
- When the empirical equations were used to predict the collision regimes of a PFI with low injection pressure, the experimental results for the collision and coalescence regimes indicated that these equations are applicable to describe droplet coalescence in a PFI of this type.
- The predicted results for droplet diameter and velocity are on the same order of magnitude as the experimental data.
- The present study provides useful insight into low pressure fuel injector of droplets undergoing collision and their associated non-linear unit processes. More investigation along these lines is needed for better understanding and modelling of droplet array.

Nomenclature

B	– impact parameter
D	– nozzle diameter [mm]
D_{new}	– diameter of the combined droplet [m]
d	– droplet diameter [mn]
m	– mass [kg]
r	– droplet radius [m]
u	– droplet velocity [ms^{-1}]
u_{12}	– relative velocity [ms^{-1}]
V	– velocity [ms^{-1}]
U_{new}	– velocity of the combined droplet [ms^{-1}]
X	– distance between the droplet centres in the direction normal to the relative velocity [m]
We	– Weber number

Greek symbols

σ	– surface tension [Nm^{-1}]
ρ	– density [Kgm^{-3}]
Δ	– droplet diameter ratio
ν	– kinematic viscosity [m^{2}s^{-1}]
ϕ'	– shape factor

Subscripts

1	– larger droplet
2	– ssmaller droplet
f	– liguid

References

[1] Nobari, M. R., *et al*., Head-on Collision of Drops – A Numerical Investigation, *Physics of Fluids*, *8* (1996), 1, pp. 29-42
[2] Ashgriz, N., Poo, J. Y., Coalescence and Separation in Binary Collisions of Liquid Drops, *Fluid Mechanics*, *221* (1990), Apr., pp. 183-204
[3] Orme, M., Experiments on Droplet Collisions, Bounce, Coalescence and Disruption, *Progress in Energy and Combustion Science*, *23* (1997) 1, pp. 65-79
[4] Qian, J., Law, C. K., Regimes of Coalescence and Separation in Droplet Collision, *Journal Of Fluid Mechanics*, *331*(1997), May, pp. 59-80
[5] Brenn, G., The formation of Satellite Droplets by Unstable Binary Drop Collisions, *Physics of Fluids*, *13* (2001), 9, pp. 2463-2477
[6] Willis, K., Orme, M., Binary Droplet Collisions in a Vacuum Environment: An Experimental Investigation of the Role of Viscosity, *Experiments in Fluids*, *34* (2003), 1, pp. 28-41
[7] Roth, N., Droplet Collision Outcomes at High Weber Number, *Proceeding*, 21st Conference of Institute for Liquid Atomization and Spray Systems, Madison, Wis., USA, 2007, pp. 10-12
[8] Pan, K. L., *et al*., Binary Droplet Collision at High Weber Number, *Physical Rev. E*, *80* (2009), 3, 36301
[9] Kuschel, M., Sommerfeld, M., Investigation of Droplet Collisions for Solutions with Different Solids Content, *Experiments in Fluids*, *54* (2013), 2, 1440
[10] Planchette, C., *et al.*, The Onset of Fragmentation in Binary Liquid Drop Collisions, *Journal of Fluid Mechanics*, *702* (2012), May, pp. 5-25
[11] Hinterbichler, H., *et al*., Ternary Drop Collisions, *Experiments in Fluids*, *56* (2015), 10, 190
[12] Post, S. L., Abraham, J., Modeling the Outcome of Drop-Drop Collisions in Diesel Sprays, *International Journal of Multiphase Flow*, *28* (2002), 6, pp. 997-1019
[13] Sommerfeld, M., Kuschel, M., Modelling Droplet Collision Outcomes for Different Substances and Viscosities, *Experiments in Fluids*, *57* (2016), 12, 187
[14] Planchette, C., *Et Al.*, Colliding Drops as Coalescing and Fragmenting Liquid Springs, *Journal of Fluid Mechanics*, *814* (2017), Feb., pp. 277-300
[15] Li, J., Macroscopic Model for Head-On Binary Droplet Collisions in a Gaseous Medium, *Physical Review Letters, 117* (2016), 21, 214502
[16] Strizhak, P. A., Characteristics of ‘Bounce’ of Interacting Water Droplets, *Technical Physics*, *64* (2019), 6, pp. 796-801
[17] Jiang, Y. J., *et al.*, An Experimental Investigation on the Collision Behaviour of Hydrocarbon Droplets, *Journal of Fluid Mechanics*, *234* (1992), Apr., pp. 171-190
[18] Pan, K. L., *et al.*, Experimental and Mechanistic Description of Merging and Bouncing in Head-On Binary Droplet Collision, *Journal of Applied Physics*, *103* (2008), 6, 64901
[19] Estrade, J. P., *et al.,* Experimental Investigation of Dynamic Binary Collision of Ethanol Droplets–A Model for Droplet Coalescence and Bouncing, *International Journal of Heat and Fluid Flow*, *20* (1999), 5, pp. 486-491
[20] Gao, T. G., *et al*., Collision Between an Ethanol Drop and a Water Drop, *Experiments in Fluids*, *38* (2005), 6, pp. 731-738

[21] Chen, R. H., Chen, C. T., Collision Between Immiscible Drops with Large Surface Tension Difference: Diesel Oil and Water, *Experiments in Fluids*, *41* (2006), 3, pp. 453-461
[22] Munnannur, A., Reitz, R. D., A New Predictive Model for Fragmenting and Non-Fragmenting Binary Droplet Collisions, *International Journal of Multiphase Flow*, *33* (2007), 8, pp. 873-896
[23] Zhang, P., Law, C. K., An Analysis of Head-On Droplet Collision with Large Deformation in Gaseous Medium, *Physics of Fluids*, *23* (2011), 4, 42102
[24] Krishnan, K. G., Loth, E., Effects of Gas and Droplet Characteristics on Drop-Drop Collision Outcome Regimes, *International Journal of Multiphase Flow*, *77* (2015), Dec., pp. 171-186
[25] Liu, D., *et al*., Collision Dynamics and Mixing of Unequal-Size Droplets," *International Journal of Heat and Mass Transfer*, *57* (2013), 1, pp. 421-428
[26] Mazloomi Moqaddam, A., *et al.,* Simulation of Binary Droplet Collisions with the Entropic Lattice Boltzmann Method, *Physics of Fluids*, *28* (2016), 2, 22106
[27] Nikolopoulos, N., Bergeles, G., The Effect of Gas and Liquid Properties and Droplet Size Ratio on the Central Collision Between Two Unequal-Size Droplets in the Reflexive Regime, *International Journal of Heat and Mass Transfer*, *54* (2011), 1, pp. 678-691
[28] Nikolopoulos, N., *et al.*, Off-Centre Binary Collision of Droplets: A Numerical Investigation, *International Journal of Heat and Mass Transfer*, *52* (2009), 19, pp. 4160-4174
[29] Nikolopoulos, N., *et al*., The Effect of Weber Number on the Central Binary Collision Outcome Between Unequal-Sized Droplets, *International Journal of Heat and Mass Transfer*, *55* (2012), 7, pp. 2137-2150
[30] Focke, C., *et al.,* Collision Between High and Low Viscosity Droplets: Direct Numerical Simulations and Experiments, *International Journal of Multiphase Flow, 56* (2013), Oct., pp. 81-92
[31] Gotaas, C., *et al.,* Effect of Viscosity on Droplet-Droplet Collision Outcome: Experimental Study and Numerical Comparison, *Physics of Fluids*, *19* (2007), 10, pp. 102-106
[32] Brazier-Smith, P. R., *et al*., The Interaction of Falling Water Drops: Coalescence. *Proceedings of the Royal Society of London. A. Mathematical and Physical Sciences*, *326* (1972), 1566, pp. 393-408.
[33] O'Rourke, P. J., Collective Drop Effects on Vaporizing Liquid Sprays, Ph. D. thesis, Los Alamos National Lab., Los Alamos, N. Mex., USA, 1981.

Paper submitted: November 11, 2019
Paper revised: May 25, 2020
Paper accepted: May 30, 2020